1   **Antibody-Based Affinity Cryo-Electron Microscopy at 2.6 Å Resolution**

2

3   Guimei Yu[1], Kunpeng Li[1], Pengwei Huang[2, 3], Xi Jiang[2, 3], Wen Jiang[1*]

4

5   [1]Markey Center for Structural Biology, Department of Biological Science, Purdue University,

6   West Lafayette, IN, USA

7   [2]Divisions of Infectious Diseases, Cincinnati Children's Hospital Medical Center, Cincinnati,

8   OH, USA

9   [3]Department of Pediatrics, University of Cincinnati College of Medicine, Cincinnati, OH, USA

10   [*]Corresponding author. Prof. Wen Jiang,

11   Email: jiang12@purdue.edu,

12   Phone: 765-496-8436

13

Abstract:

15 The affinity cryo-electron microscopy (cryo-EM) approach has been explored in recent years to

16 simplify and improve the sample preparation for cryo-EM. Despite the demonstrated successes

17 for low-concentration and unpurified specimens, the lack of near-atomic structures using this

18 approach has led to a common perception of affinity cryo-EM as a niche technique incapable of

19 reaching high resolutions. Here, we report a ~2.6 Å structure solved using the antibody-based

20 affinity grid approach with a Tulane virus sample of low concentration. This is the first near-

21 atomic structure solved using the affinity cryo-EM approach. Quantitative analyses of the

22 structure indicate data and reconstruction quality comparable to conventional grid preparation

23 method using samples at high concentration. With the shifting of bottlenecks of cryo-EM

24 structural studies to sample grid preparation, our demonstration of the sub-3 Å capability of

25 affinity cryo-EM approach indicates its potential in revolutionizing cryo-EM sample preparation

26 for a broader spectrum of specimens.

27

28

29

30

31

32

33 **Key words:** antibody-based affinity grid; affinity cryo-electron microscopy; single particle 3D

34 reconstruction; Tulane Virus

35

36 **Introduction:**

37 The remarkably improved image quality provided by direct electron detectors, together with

38 other hardware and software advances, have resulted in an explosion of near-atomic resolution

39 structures determined by single particle cryo-EM (Bai et al., 2015; Banerjee et al., 2016;

40 Bartesaghi et al., 2015; Campbell et al., 2015; Grant and Grigorieff, 2015; Merk et al., 2016;

41 Wang et al., 2014). Furthermore, the recent breakthrough in the Volta phase plate technique

42 (Danev and Baumeister, 2016; Khoshouei et al., 2016) holds great promise to extend single

43 particle cryo-EM to more samples with molecular masses below 100 KDa. Since microscopes,

44 detectors, and image processing algorithms are no longer bottlenecks, the major hurdles for most

45 cryo-EM projects have now shifted to sample grid preparation, which usually consists of a multi-

46 step sample purification process and the subsequent preparation of a thin film of frozen-hydrated

47 sample on TEM grids (Grassucci et al., 2007). Further innovation in cryo-EM sample grid

48 preparation is of great significance for developing single particle cryo-EM into a routine

49 structural biology tool. The affinity cryo-EM approach that modifies TEM grids with an extra

50 affinity layer to immobilize, purify, and concentrate target samples possesses a great potential to

51 simplify and improve the cryo-EM grid preparation for a broader range of specimens, such as

52 those of low yield and unpurified samples (Glaeser, 2015; Taylor and Glaeser, 2008; Yu et al.,

53 2016a).

54 Multiple affinity cryo-EM approaches based on different types of affinity layers including

55 functionalized lipid layer (Azubel et al., 2004; Benjamin et al., 2016; Kelly et al., 2008; Medalia

56 et al., 2002), 2D crystals of streptavidin (Han et al., 2012), antibody layer (Yu et al., 2014) and

57 chemically functionalized carbon surface (Llaguno et al., 2014) have been reported. The affinity

3

58   cryo-EM method provides various advantages. First, it enables single particle cryo-EM studies of

59   low-concentration samples that are often encountered due to low abundance in natural sources,

60   low yield of expression systems, or safety concerns for highly contagious/dangerous pathogens.

61   Secondly, it allows direct isolation of target particles from crude extracts via a specific

62   interaction (Kelly et al., 2008; Yu et al., 2014), which combines sample purification with grid

63   setup, simplifying cryo-EM grid preparation into a single-step process. Moreover, better sample

64   integrity can be obtained for labile macromolecular complexes with affinity cryo-EM approaches

65   by avoiding multiple biochemical purification steps. Finally, immobilization of particles to an

66   affinity layer can reduce particle diffusion and minimize potential sample damages at the air-

67   water interface during and after sample blotting (Taylor and Glaeser, 2008). Altogether, these

68   benefits of affinity cryo-EM will potentially bring more samples within reach of single particle

69   cryo-EM, and also provide a more convenient, higher throughput, and mild cryo-EM grid

70   preparation method.

71   Although multiple 3-D reconstructions have been reported with affinity cryo-EM

72   approaches (Han et al., 2012; Kelly et al., 2008; Llaguno et al., 2014; Yu et al., 2014; Zhang et

73   al., 2015), these structures were all limited to low to intermediate resolutions and no near-atomic

74   reconstructions have been obtained. Thereby there has been a common worry about using

75   affinity cryo-EM approach for high-resolution single particle reconstructions, which prohibits the

76   widespread use of the affinity cryo-EM approach. Tulane virus (TV) is a monkey calicivirus in

77   the *recovirus* genus of the *caliciviridae* and serves as a surrogate for human norovirus studies

78   (Wei et al., 2008; Yu et al., 2013). Due to the low yield, the purified TV particles from cell

79   cultures were often at a concentration of $\sim 10^{10\text{-}11}$ particles/ml, which is too low for conventional

80 cryo-EM studies that usually need ~10^{14} particles/ml or higher for most viral samples. In this

81 work, we have used this challenging low-concentration TV sample to explore the potential of

82 using antibody-based affinity grid for high-resolution cryo-EM. By concentrating TV particle via

83 the anti-TV antibody affinity layer on the grid, and also optimizing the cryo-EM grid freezing

84 condition to achieve an optimal freezing where particles of interest immobilized on the antibody-

85 affinity layer were frozen in vitreous ice with a thickness slightly larger than the particle size, we

86 have obtained high quality cryo-EM data for TV particles. A ~2.6 Å structure of TV was solved

87 using the antibody-based affinity cryo-EM approach, which for the first time demonstrated the

88 ability of affinity cryo-EM approach for solving sub-3 Å structures.

89

90 **Results and Discussion:**

91 TEM grids were coated with anti-TV IgGs aided by protein A as described previously (Yu

92 et al., 2016a, 2014). As expected, TV particles were immobilized and concentrated efficiently on

93 the anti-TV antibody-coated TEM grid to a level allowing for cryo-EM grid preparation (figure

94 s1). Cryo-EM sample of TV on the antibody-coated affinity grid was prepared using perforated

95 carbon grids layered with thin continuous carbon (Figure 1A). The extra affinity layer brings

96 more background noise to cryo-EM images relative to standard cryo-EM grids, which is

97 essentially the major reason for the common concern about applying affinity cryo-EM for high-

98 resolution cryo-EM reconstruction. The extra noises from the affinity layer cannot be

99 computationally removed in most affinity cryo-EM approaches (Kelly et al., 2008; Llaguno et

100 al., 2014; Yu et al., 2014). However, such loss of image contrast due to the affinity layer can be

101 compensated by reducing the ice thickness without exposing the immobilized particles to the air-

102   water interface. For example, reducing ice thickness by ~30 nm could theoretically balance out

103   the extra electron scattering by an affinity layer formed by protein A and IgGs (~13 nm in

104   thickness) on the carbon film (~3 nm) (Vulović et al., 2013).   Therefore, to pursue the best

105   possible affinity cryo-EM images, freezing conditions were screened for an optimal ice thickness

106   that is slightly larger than the size of TV particle (~40 nm).

107   Since visual evaluation of ice thickness in the range of tens to hundreds of nanometers (e.g.,

108   50-150 nm) is challenging, quantitative estimation of ice thickness is necessary. An ice thickness

109   measurement method based on the Beer-Lambert law was adopted (Yan et al., 2015), in which

110   the ice thickness (t) can be approximated from the ratio of image intensity of a melted area (I_0)

111   and an area with ice (I), and the inelastic mean free path of electrons in vitreous ice (λ_{in}) using

112   the equation $t = \lambda_{in} ln\left(\frac{I_0}{I}\right)$. Mean image intensities (I_0 and I) can be measured directly using the

113   DigitalMicrograph software (Gatan, Inc.) controlling the camera, which allows convenient on-

114   line measurement of ice thickness during sample screening. The quantitative estimation of ice

115   thicknesses allowed successful optimization of ice thickness with obviously improved image

116   contrast (figure s2). A sample freezing condition producing vitreous ice with an estimated

117   thickness of ~40-70 nm was obtained for TV particles on the anti-TV antibody-coated grid

118   (Figure 1B,C). Cryo-EM movies of TV were collected automatically by using Leginon

119   (Carragher et al., 2000) to control the FEI Titan Krios microscope and the Gatan K2 Summit

120   direct electron detector. For most movies, signals at 4 Å or higher resolutions were recovered

121   after motion correction (Figure 1E,F).

122   Single particle analysis was performed using *jspr* program (Guo and Jiang, 2014). The truly

123   independent image processing strategy was adopted, in which the whole dataset was split into

124   two halves and processed completely independently (Guo and Jiang, 2014; Liu et al., 2016).

125   Based on the 0.143 cutoff criterion of gold-standard Fourier shell correlation (FSC) curve, a final

126   3-D reconstruction of TV at an overall resolution of 2.6 Å was obtained from ~14K particles

127   (Figure 2A,B). As shown in Figure 2A, TV structure contains two major density layers, the basal

128   shell layer (green-colored) and the protruding layer (blue-colored). Conformational flexibility

129   has been suggested for the protruding layer of TV and TV-related structures (Chen et al., 2006;

130   Katpally et al., 2010; Prasad, 1999; Yu et al., 2013). To evaluate the resolutions of the two

131   layers, FSC curves were calculated for the shell layer and the protruding layer, respectively. As

132   expected, the shell layer with an estimated resolution of ~2.5 Å was better resolved than the

133   more flexible protruding layer (~2.7 Å) (Figure 2B). Analysis of the determined Euler angles of

134   TV particles revealed a uniform coverage of the angle space (figure s3), suggesting that no view

135   preference was introduced by the antibody affinity layer.

136   To further evaluate the quality of this affinity cryo-EM TV dataset and 3-D reconstruction,

137   its overall B factor ($B_{overall}$) was approximated. $B_{overall}$, which reflects the composite effect of

138   sample integrity and homogeneity, ice thickness, imaging quality and computing errors, is a good

139   indicator of cryo-EM data and 3-D reconstruction quality (Liu et al., 2007; Rosenthal and

140   Richard, 2003). Based on the linear relationship between $2ln(N_{asu}d)$ and $1/d^2$, in which N_{asu} is the

141   number of asymmetric units used for the 3-D reconstruction and d is the resolution, $B_{overall}$ is

142   equal to the slope of the linear fitting (Rosenthal and Richard, 2003). As shown in Figure 2C, the

143    $2ln(N_{asu}d)-1/d^2$ plot of this affinity cryo-EM TV dataset showed an apparent linear relationship

144   and yielded a $B_{overall}$ of 104 Å^2. This $B_{overall}$ is smaller than previously reported $B_{overall}$ for

145   structures determined at 3.2 to 7 Å resolutions (Danev and Baumeister, 2016; Liu et al., 2007;

7

146   Wang et al., 2014), which further confirms the excellent overall quality of this TV dataset.

147   Moreover, we reprocessed a published cryo-EM dataset of 20S proteasome (Campbell et al.,

148   2015) in the same way as for TV using *jspr* and obtained a 3-D reconstruction of ~2.7 Å (figure

149   s4). The 20S proteasome data was collected under similar imaging conditions as TV (i.e., Titan

150   Krios and Gatan K2 Summit) but using standard holey grids and samples. The plot of $2ln(N_{asu}d)$-

151     $1/d^2$ for the 20S proteasome yielded a $B_{overall}$ of 111 Å (Figure 2D) that is comparable to the

152     $B_{overall}$ of the affinity cryo-EM TV dataset. This comparison suggests that the antibody-based

153   affinity grid approach can not only provide cryo-EM grids of similar quality (if not better) as the

154   standard cryo-EM grid preparation approach, but also provide distinct advantages for those

155   samples beyond reach of standard single particle cryo-EM.

156   With our ~2.6 Å 3-D reconstruction of TV, many high-resolution structural features were

157   resolved (Figure 3). Figure 3 shows three representative regions of TV density map including a

158   short α-helix followed by a loop (Figure 3A) and two β-strands (Figure 3B,C), in which side

159   chain densities can be easily recognized for most residues. Both hydroxyl groups in Tyr residues

160   and the backbone carbonyl oxygen atoms are distinguishable (Figure 3A to C). In addition, this

161   high-quality map of TV also allowed unambiguous assignment of rotameric conformations of

162   most side chains. For example, different rotamers of Ile residues were unambiguously identified

163   based on the density (Figure 3D) and the correct rotamers were distinguishable from multiple

164   similar rotameric states (Figure 3E). Many ordered water molecules were also observed to form

165   hydrogen bonds with neighboring residues or other water molecules (Figure 3F).

166   In conclusion, by optimizing the cryo-EM grid preparation condition to plunge-freeze the

167   immobilized particles on the antibody-affinity layer in vitreous ice with a thickness slightly

168   larger than the particle size, we have obtained high-quality cryo-EM data for TV and solved a

169   ~2.6 Å structure using the antibody-based affinity cryo-EM approach. This demonstrates the

170   feasibility of using the antibody-based affinity cryo-EM approach for sub-3 Å structures and

171   suggests the potential of using affinity cryo-EM approach as a more efficient and robust way of

172   grid preparation for high-resolution cryo-EM. With antibodies commercially available for a vast

173   number of samples, the antibody-based affinity cryo-EM method can potentially revolutionize

174   cryo-EM sample preparation for a broader spectrum of native specimens, at least for most viral

175   samples as demonstrated in this work. Optimization and demonstration of the antibody-based

176   affinity cryo-EM approach for high resolution structure determination of smaller protein

177   complexes will be performed in the near future for more general usage of this approach in cryo-

178   EM.

179

Materials and methods:

Purification of TV

182   TV was purified as described previously with some modifications (Yu et al., 2013). Briefly,

183   LLC-MK2 cells (ATCC, Manassas, VA) grown to 80-90% confluency were inoculated with TV

184   at a multiplicity of infection (MOI) of 0.2. Cells were collected after 72 hours and subject to

185   three freeze-thaw cycles to release progeny TV. After clarifying by centrifugation at 13,776× g

186   to remove cell debris, the supernatant was centrifuged at 28,000 rpm (SW28 rotor, Beckman,

187   Danvers, MA). The pellet was suspended and further clarified by 20% (w/v) sucrose cushion

188   ultracentrifugation at 28,000 rpm for 4 hours. Finally, the pellet was suspended and applied to a

189   CsCl density gradient centrifugation at 288,000× g for 45 h (SW41Ti rotor, Beckman, Danvers,

190   MA). The fractions containing TV virion were collected. Plaque assay was performed and

191   revealed a titer of ~10^8 plaque forming units (PFU)/ml. Sample was dialyzed against 1×PBS

192   buffer (137 mM NaCl, 2.7 mM KCl, 10 mM phosphate, pH 7.4) for use.

193   **Preparation of antibody-coated TEM grids**

194   The amorphous carbon layer of TEM grids was coated with antibodies as described before (Yu et

195   al., 2016a, 2014). The protein A-aided antibody coating method was applied in this work.

196   Briefly, homemade Formvar/carbon grids or commercial grids layered with lacey carbon and

197   ultrathin continuous carbon (e.g., Ted Pella #01824) were glow-discharge cleaned for ~40 s at 15

198   mA current and 0.2-0.15 Torr vacuum using a Ladd vacuum evaporator (Ladd Research,

199   Williston, VT). 5 µl of 50 µg/ml Protein A (Sigma Aldrich) was applied to the cleaned carbon

200   surface and incubated for ~10-15 min at room temperature. After removing the excess liquids, 5

201   µl of diluted antiserum was quickly applied to the grid and incubated for 15-20 min in a humid

202   chamber at ambient temperature. The residual liquid and unbound antibody were blotted away,

203   and the grid was subjected to 30s washing with 100-200 µl of 1×PBS buffer (pH 7.4).

204   **Ice thickness estimation**

205   Cryo-EM grids of frozen sample under different conditions were checked using a Philips CM200

206   microscope with a 1K CCD camera. The overall quality of the frozen grids were first visually

207   evaluated as usual (Grassucci et al., 2007); For those promising conditions, the ice thickness was

208   quantitatively estimated using the thickness estimation method based on Beer-Lambert law

209   (Malis et al., 1988; Yan et al., 2015). More specifically, after melting the ice at a corner of the

210   vitreous ice film, a low-magnification image (e.g., 3,800×) was taken covering both the region of

211   interest and the melted area using a CCD camera. Beam intensities without (I_0) and with (I) ice

212 scattering, and inelastic mean free path of electrons in vitreous ice (λ_{in}) determine the ice

213 thickness: $t = \lambda_{in} ln \left(\frac{I_0}{I}\right)$. Since I_0 and I can be measured directly using the DigitalMicrograph

214 software (Gatan, Inc.) controlling the camera during sample screening, it provides immediate

215 feedback for the ice thickness optimization. λ_{in} of 300 nm was used for the microscope operated

216 at 200 KV as estimated in the references (Vulović et al., 2013; Yan et al., 2015).

217 **Affinity cryo-EM grid preparation and data collection of TV**

218 TEM grids layered with lacey carbon support and a continuous ultrathin carbon (Ted Pella

219 #01824) were coated with anti-TV antiserum (1:10 diluted, (Yu et al., 2014)) as described above.

220 3 µl of the purified TV sample was applied to the grid-coated with anti-TV antibody, and

221 incubated in a humid chamber at 4 °C for ~30 min. Due to the limited amount of purified TV

222 sample, only 3 µl sample was applied per grid. The grid was washed for ~2 min by floating on a

223 drop of 200 µl cold 1×PBS, pH7.4, and plunge-frozen using a Gatan Cp3 (or FEI Vitrobot) cryo-

224 plunger. Different cryo-EM grid freezing conditions (e.g., blotting time, humidity) were

225 attempted and evaluated visually complemented by quantitative ice thickness estimation as

226 aforementioned. A freezing condition leading to vitreous ice of ~60 nm on average for TV was

227 identified. A dataset of ~1,000 movies was collected using FEI Titan Krios TEM operating at

228 300 KV and liquid nitrogen temperature, and recorded with the Gatan K2 Summit direct electron

229 detector at super-resolution movie mode (5 frames/second) at 225,00× nominal magnification

230 (0.65 Å/super-pixel). A dose rate of 8 electrons/physical pixel/second and a total exposure of 5

231 seconds resulted in a total dose of ~21 e/Å^2 for the collected images.

232 **Single particle 3-D reconstruction using *jspr***

233   A script *motionCorrect.py* that runs the *dosefgpu_driftcorr* program (Li et al., 2013) in batch

234   mode was used to determine motions among raw movie frames

235   (https://github.com/jianglab/motioncorr). ~20,000 particles were selected from motion-corrected

236   movie sums using RELION automatic particle picking module (Scheres, 2012). The *jspr*

237   program *batchboxer.py* (Guo and Jiang, 2014; Liu et al., 2016) was used to extract the particles

238   from raw movie frames based on the particle coordinates files, the frame shift parameters

239   determined by *motionCorrect.py,* and the total electron dose. The extracted particles were both

240   motion-corrected and dose-weighted adopting the radiation damage compensation strategy

241   described in reference (Wang et al., 2014). The particle images were resampled from 0.650 to

242   0.975 Å/pixel using the Fourier cropping method. The *jspr* program *fitctf2.py* (Jiang et al., 2012)

243   was used to determine the initial CTF parameters from the extracted particles. The estimation

244   and correction of astigmatism aberration was performed later during iterative refinement using

245   the aligner *refineAstigmatism* in *jspr* (Guo and Jiang, 2014; Liu et al., 2016). The whole dataset

246   was then split into two half datasets, even and odd subsets, which were processed independently,

247   including constructions of *de novo* initial models and subsequent refinements as described before

248   (Guo and Jiang, 2014; Liu et al., 2016). Three correct *de novo* initial models were obtained using

249   the random model method (Guo and Jiang, 2014; Liu et al., 2016) for both the "even" and "odd"

250   halves, respectively, which were used as initial references to determine the Euler/Center

251   parameters of all particles. This resulted in three sets of Euler/center parameters for each particle,

252   based on which particles with consensus Euler/Center parameters were selected for further

253   refinement. In the *jspr* program (Guo and Jiang, 2014), in addition to Euler/Center searching,

254   many potential modulations present in 2-D images are also formulated as 2-D alignment tasks

255   (often referred to as high-order alignments), including micrograph and per-particle defocus,

256   astigmatism aberration, overall scale variance among 2-D images, elliptic magnification

257   distortion, and phase error from residual coma (Guo and Jiang, 2014; Liu et al., 2016; Yu et al.,

258   2016b). Initial refinement was performed with only the Euler/Center parameters. After the

259   convergence of the orientation/center refinement at ~3.6 Å, high-order aligners were gradually

260   added to the iterative refinement loop to determine and correct those image artifacts as

261   aforementioned, which all together improved the quality of the 3-D reconstruction to ~2.6 Å.

262   The 0.143 cutoff for gold-standard Fourier Shell Correlation (FSC) curve (Rosenthal and

263   Richard, 2003) was used to estimate the resolution of reconstruction with "even" and "odd"

264   maps soft-masked using EMAN2 (Tang et al., 2007) adaptive masking processor (*mask.auto3d*).

265   The final map of TV was reconstructed from 14,154 particles by pooling the two half datasets.

266   The final map was sharpened using the 1D structure factor of TV fitted from the images, and a

267   low pass filter derived from the final FSC curve to boost the high-resolution Fourier amplitudes,

268   and to suppress the high-frequency noise, respectively (Guo and Jiang, 2014; Rosenthal and

269   Richard, 2003).

270   **Estimation of overall B factor ($B_{overall}$) of cryo-EM data and reconstruction**

271   Different numbers of particles were randomly selected from final refinement particle sets. New

272   3-D reconstructions were performed and the resolutions were estimated based on gold-standard

273   FSC curves. The number of particles for 3-D reconstructions was then plotted against the

274   corresponding achievable resolutions. Specifically, the *$2ln(N_{asu}d)$* as a function of *$1/d^2$* was

275   plotted, in which N_{asu} is the number of asymmetric units and *d* is the achievable resolution of 3-D

276   reconstructions. Based on the mathematical formulation of the relationship of N_{asu}, d and the

13

277   $B_{overall}$ (Figure 11 in (Rosenthal and Richard, 2003)), $B_{overall}$ can be approximated as the slope of

278   the linear fitting of *2ln(N_{asu}d)* and *1/d²*.

279

Acknowledgements:

281   This work was supported by NIH grant (1R01AI111095). Both negative staining and cryo-EM

282   images were taken at Purdue Cryo-EM Facility. We thank Dr. Philip Serwer for providing the

283   bacteriophage T7 antiserum, and Frank Vago for proofreading the manuscript.

284

References:

286   Azubel, M., Wolf, S.G., Sperling, J., Sperling, R., 2004. Three-dimensional structure of the

287   native spliceosome by cryo-electron microscopy. Mol. Cell 15, 833–839.

288   Bai, X.-C., Rajendra, E., Yang, G., Shi, Y., Scheres, S.H.W., 2015. Sampling the conformational

289   space of the catalytic subunit of human γ-secretase. Elife 4. doi:10.7554/eLife.11182

290   Banerjee, S., Bartesaghi, A., Merk, A., Rao, P., Bulfer, S.L., Yan, Y., Green, N., Mroczkowski,

291   B., Neitz, R.J., Wipf, P., Falconieri, V., Deshaies, R.J., Milne, J.L.S., Huryn, D., Arkin, M.,

292   Subramaniam, S., 2016. 2.3 Å resolution cryo-EM structure of human p97 and mechanism

293   of allosteric inhibition. Science. doi:10.1126/science.aad7974

294   Bartesaghi, A., Merk, A., Banerjee, S., Matthies, D., Wu, X., Milne, J.L.S., Subramaniam, S.,

295   2015. 2.2 Å resolution cryo-EM structure of β-galactosidase in complex with a cell-

296   permeant inhibitor. Science 348, 1147–1151.

297   Benjamin, C.J., Wright, K.J., Seok-Hee, H., Kyle, K., Guimei, Y., Ruchika, B., Fei, G.,

298   Stauffacher, C.V., Wen, J., Thompson, D.H., 2016. Nonfouling NTA-PEG-Based TEM

14

299   Grid Coatings for Selective Capture of Histidine-Tagged Protein Targets from Cell Lysates.

300   Langmuir 32, 551–559.

301   Campbell, M.G., Veesler, D., Cheng, A., Potter, C.S., Carragher, B., 2015. 2.8 Å resolution

302   reconstruction of the Thermoplasma acidophilum 20S proteasome using cryo-electron

303   microscopy. Elife 4. doi:10.7554/eLife.06380

304   Carragher, B., Bridget, C., Nick, K., David, K., Milligan, R.A., Potter, C.S., James, P., Amy, R.,

305   2000. Leginon: An Automated System for Acquisition of Images from Vitreous Ice

306   Specimens. J. Struct. Biol. 132, 33–45.

307   Chen, R., Neill, J.D., Estes, M.K., Prasad, B.V.V., 2006. X-ray structure of a native calicivirus:

308   Structural insights into antigenic diversity and host specificity. Proceedings of the National

309   Academy of Sciences 103, 8048–8053.

310   Danev, R., Baumeister, W., 2016. Cryo-EM single particle analysis with the Volta phase plate.

311   Elife 5. doi:10.7554/eLife.13046

312   Glaeser, R.M., 2015. How good can cryo-EM become? Nat. Methods 13, 28–32.

313   Grant, T., Grigorieff, N., 2015. Measuring the optimal exposure for single particle cryo-EM

314   using a 2.6 Å reconstruction of rotavirus VP6. Elife 4, e06980.

315   Grassucci, R.A., Taylor, D.J., Joachim, F., 2007. Preparation of macromolecular complexes for

316   cryo-electron microscopy. Nat. Protoc. 2, 3239–3246.

317   Guo, F., Jiang, W., 2014. Single Particle Cryo-electron Microscopy and 3-D Reconstruction of

318   Viruses, in: Kuo, J. (Ed.), Electron Microscopy, Methods in Molecular Biology . Humana

319   Press, pp. 401–443.

320   Han, B.-G., Bong-Gyoon, H., Walton, R.W., Amos, S., Peter, H., Stubbs, M.T., Yannone, S.M.,

15

321   Pablo, A., Ming, D., Glaeser, R.M., 2012. Electron microscopy of biotinylated protein
322   complexes bound to streptavidin monolayer crystals. J. Struct. Biol. 180, 249–253.

323 Jiang, W., Guo, F., Liu, Z., 2012. A graph theory method for determination of cryo-EM image
324   focuses. J. Struct. Biol. 180, 343–351.

325 Katpally, U., Voss, N.R., Cavazza, T., Taube, S., Rubin, J.R., Young, V.L., Stuckey, J., Ward,
326   V.K., Virgin, H.W., 4th, Wobus, C.E., Smith, T.J., 2010. High-resolution cryo-electron
327   microscopy structures of murine norovirus 1 and rabbit hemorrhagic disease virus reveal
328   marked flexibility in the receptor binding domains. J. Virol. 84, 5836–5841.

329 Kelly, D.F., Dukovski, D., Walz, T., 2008. Monolayer purification: A rapid method for isolating
330   protein complexes for single-particle electron microscopy. Proceedings of the National
331   Academy of Sciences 105, 4703–4708.

332 Khoshouei, M., Radjainia, M., Phillips, A.J., Gerrard, J.A., Mitra, A.K., Plitzko, J.M.,
333   Baumeister, W., Danev, R., 2016. Volta phase plate cryo-EM of the small protein complex
334   Prx3. Nat. Commun. 7, 10534.

335 Liu, X., Xiangan, L., Wen, J., Joanita, J., Wah, C., 2007. Averaging tens to hundreds of
336   icosahedral particle images to resolve protein secondary structure elements using a Multi-
337   path Simulated Annealing optimization algorithm. J. Struct. Biol. 160, 11–27.

338 Liu, Z., Guo, F., Wang, F., Li, T.C., Jiang, W., 2016. 2.9 Angstrom Resolution Cryo-EM 3-D
339   Reconstruction of Close-packed PCV2 Virus-like Particles. Structure 24, 319–328.

340 Li, X., Mooney, P., Zheng, S., Booth, C.R., Braunfeld, M.B., Gubbens, S., Agard, D.A., Cheng,
341   Y., 2013. Electron counting and beam-induced motion correction enable near-atomic-
342   resolution single-particle cryo-EM. Nat. Methods 10, 584–590.

343   Llaguno, M.C., Hui, X., Liang, S., Nian, H., Hong, Z., Qinghua, L., Qiu-Xing, J., 2014.

344   Chemically functionalized carbon films for single molecule imaging. J. Struct. Biol. 185,

345   405–417.

346   Malis, T., Cheng, S.C., Egerton, R.F., 1988. EELS log-ratio technique for specimen-thickness

347   measurement in the TEM. J. Electron Microsc. Tech. 8, 193–200.

348   Medalia, O., Typke, D., Hegerl, R., Angenitzki, M., Sperling, J., Sperling, R., 2002.

349   Cryoelectron microscopy and cryoelectron tomography of the nuclear pre-mRNA

350   processing machine. J. Struct. Biol. 138, 74–84.

351   Merk, A., Bartesaghi, A., Banerjee, S., Falconieri, V., Rao, P., Davis, M.I., Pragani, R., Boxer,

352   M.B., Earl, L.A., Milne, J.L.S., Subramaniam, S., 2016. Breaking Cryo-EM Resolution

353   Barriers to Facilitate Drug Discovery. Cell. doi:10.1016/j.cell.2016.05.040

354   Prasad, B.V.V., 1999. X-ray Crystallographic Structure of the Norwalk Virus Capsid. Science

355   286, 287–290.

356   Rosenthal, P.B., Richard, H., 2003. Optimal Determination of Particle Orientation, Absolute

357   Hand, and Contrast Loss in Single-particle Electron Cryomicroscopy. J. Mol. Biol. 333,

358   721–745.

359   Scheres, S.H.W., 2012. RELION: implementation of a Bayesian approach to cryo-EM structure

360   determination. J. Struct. Biol. 180, 519–530.

361   Tang, G., Peng, L., Baldwin, P.R., Mann, D.S., Jiang, W., Rees, I., Ludtke, S.J., 2007. EMAN2:

362   an extensible image processing suite for electron microscopy. J. Struct. Biol. 157, 38–46.

363   Taylor, K.A., Glaeser, R.M., 2008. Retrospective on the early development of cryoelectron

364   microscopy of macromolecules and a prospective on opportunities for the future. J. Struct.

365   Biol. 163, 214–223.

366   Vulović, M., Miloš, V., Ravelli, R.B.G., van Vliet, L.J., Koster, A.J., Ivan, L., Uwe, L., Hans, R.,

367   Ozan, Ö., Bernd, R., 2013. Image formation modeling in cryo-electron microscopy. J.

368   Struct. Biol. 183, 19–32.

369   Wang, Z., Hryc, C.F., Bammes, B., Afonine, P.V., Jakana, J., Chen, D.-H., Liu, X., Baker, M.L.,

370   Kao, C., Ludtke, S.J., Schmid, M.F., Adams, P.D., Chiu, W., 2014. An atomic model of

371   brome mosaic virus using direct electron detection and real-space optimization. Nat.

372   Commun. 5, 4808.

373   Wei, C., Farkas, T., Sestak, K., Jiang, X., 2008. Recovery of infectious virus by transfection of in

374   vitro-generated RNA from tulane calicivirus cDNA. J. Virol. 82, 11429–11436.

375   Yan, R., Edwards, T.J., Pankratz, L.M., Kuhn, R.J., Lanman, J.K., Liu, J., Jiang, W., 2015.

376   Simultaneous determination of sample thickness, tilt, and electron mean free path using

377   tomographic tilt images based on Beer–Lambert law. J. Struct. Biol. 192, 287–296.

378   Yu, G., Li, K., Jiang, W., 2016a. Antibody-based affinity cryo-EM grid. Methods.

379   doi:10.1016/j.ymeth.2016.01.010

380   Yu, G., Li, K., Liu, Y., Chen, Z., Wang, Z., Yan, R., Klose, T., Tang, L., Jiang, W., 2016b. An

381   Algorithm for Estimation and Correction of Anisotropic Magnification Distortion of Cryo-

382   EM Images without Need of Pre-calibration. J. Struct. Biol. doi:10.1016/j.jsb.2016.06.003

383   Yu, G., Vago, F., Zhang, D., Snyder, J.E., Yan, R., Zhang, C., Benjamin, C., Jiang, X., Kuhn,

384   R.J., Serwer, P., Thompson, D.H., Jiang, W., 2014. Single-step antibody-based affinity

385   cryo-electron microscopy for imaging and structural analysis of macromolecular

386   assemblies. J. Struct. Biol. 187, 1–9.

387   Yu, G., Zhang, D., Guo, F., Tan, M., Jiang, X., Jiang, W., 2013. Cryo-EM Structure of a Novel

388   Calicivirus, Tulane Virus. PLoS One 8, e59817.

389   Zhang, C., Vago, F., Guo, F., Liu, Z., Yu, G., Serwer, P., Jiang, W., 2015. Affinity Cryo-

390   Electron Microscopy Studies of Viral Particles Captured Directly from Cell Culture.

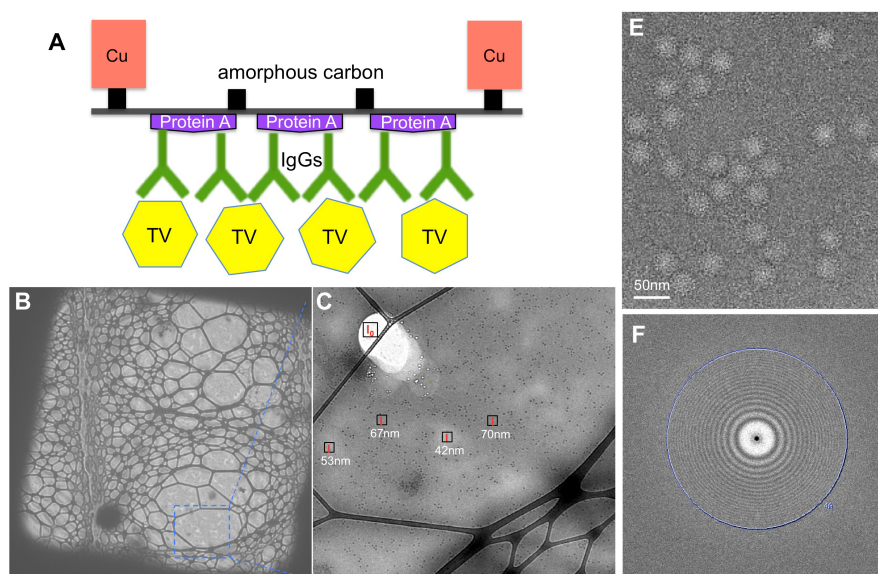391   Microsc. Microanal. 21, 547–548.

392

Figures

Figure 1. Antibody-based affinity cryo-EM of TV. (A) Schematic diagram of TV immobilized on the antibody-based affinity grid. For clear visualization, it was not drawn to scale. (B-C) Affinity cryo-EM micrographs of TV frozen using the optimized condition at 500× (B) and 3,800× (C) magnifications. Local ice thicknesses were estimated using the Beer-Lambert law based method. (E) A representative motion-corrected micrograph. (F) The 2-D power spectrum of the micrograph in (E). The position of 4 Å is labeled.
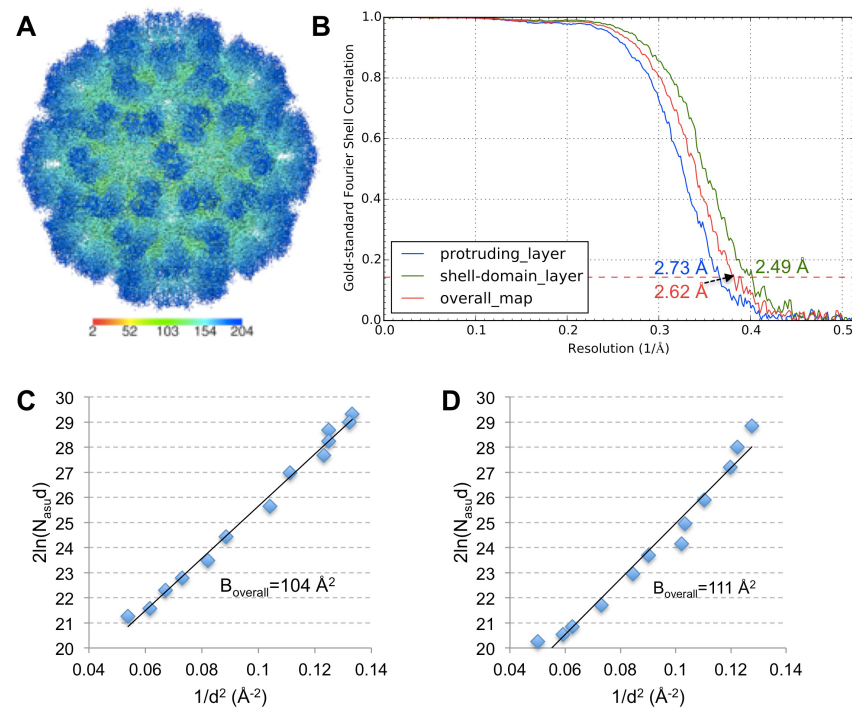
Figure 2. Single particle 3-D reconstruction of TV using affinity cryo-EM data. (A) Surface representation of TV radially colored according to the provided color key. (B) Gold-standard FSC curves of the overall map (red), the protruding layer (blue) and the shell layer (green). The position of the 0.143 FSC cutoff for resolution estimation is labeled with a dashed line. (C, D) *2ln(N_{asu}d)* vs *1/d²* is plotted for $B_{overall}$ estimation of the affinity cryo-EM data of TV (C) and the cryo-EM dataset of 20S proteasome (EMPIAR-10025) re-processed using *jspr* (D), respectively.
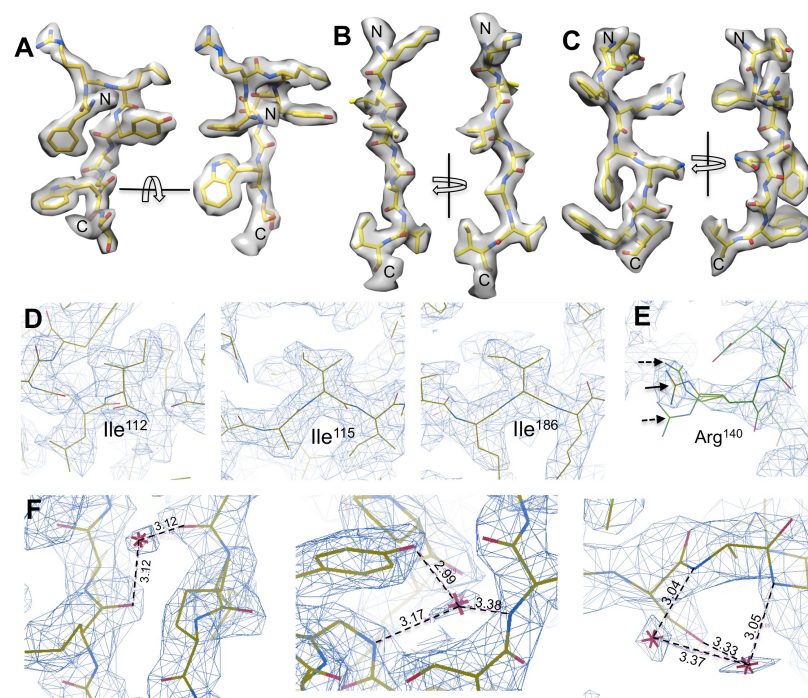
Figure 3. Atomic structural features resolved in the ~2.6 Å map of TV. (A) Densities for a short α-helix followed by a short loop. (B, C) Densities for two β-strands. (D) Multiple rotameric states identified for Ile residues. (E) shows one example of distinguishing the correct rotamer (solid arrow) from alternative rotameric states (dashed arrow) for residue Arg[140]. (F) Water molecules resolved in TV map. Water molecules were only assigned to densities present in both maps generated using the two half datasets. Hydrogen bonds were shown in dashed lines with the bond length labeled.

Supplementary Figures:
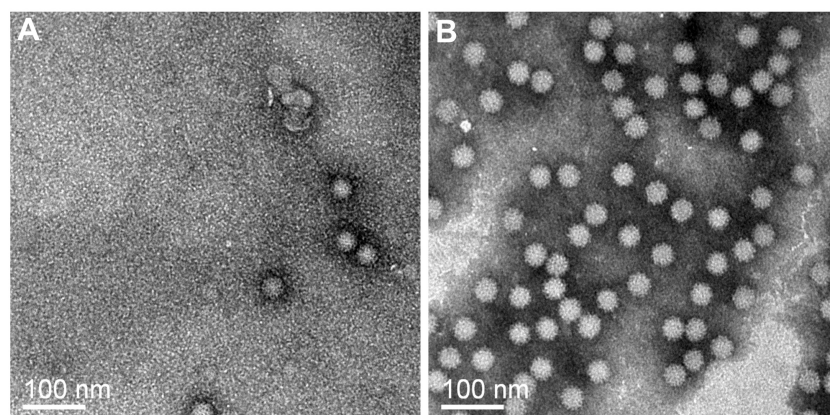
Figure s1. Negative stain TEM images of TV. (A) TV on regular TEM grid without affinity layer. (B) TV on the protein A-antiTV coated affinity grid. 3µl of purified TV sample was used to prepare both grids. Negative staining was performed with 2% phosphotungstic acid (PTA) at pH7.0.
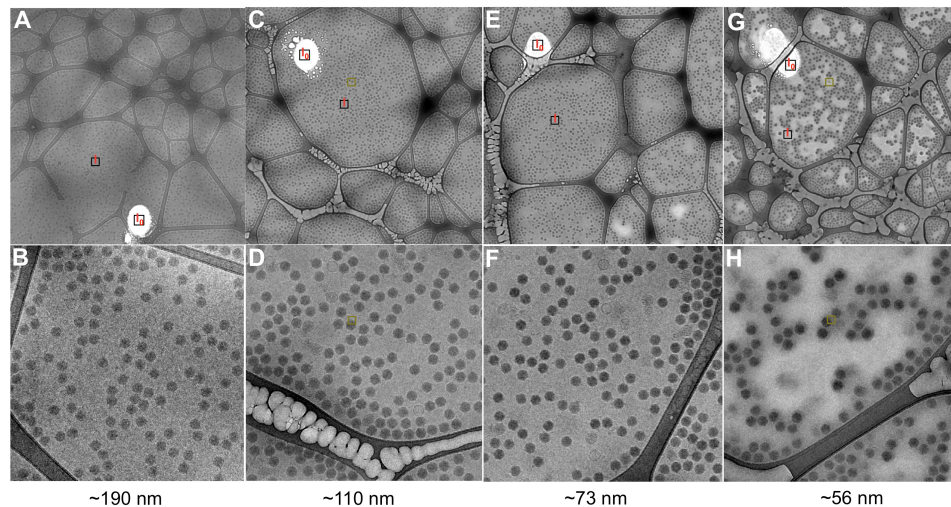

Figure s2. Optimization of cryo-freezing conditions of antibody affinity grids. Due to the limited amount of TV sample, the initial ice thickness optimization tests were performed using bacteriophage T7 that is available in large quantity in the lab. Affinity cryo-EM grids of bacteriophage T7 were prepared with protein A and anti-T7 antiserum as described in *Methods*.

(A, C, E and G) show low magnification images of grids using four different freezing conditions. "I_0" indicates the image intensities at the areas with ice melted away, and "I" represents intensities at areas with ice. The ice thickness of these four conditions was estimated at 190 nm, 110 nm, 73 nm and 56 nm, respectively, using the Beer-Lambert law based ice thickness estimation method. (B, D, F and G) show corresponding higher magnification micrographs of above four grids. Reduction of ice thickness correlated with the improvement of image contrast. The grid for micrograph G/H was slightly over-blotted that resulted in ice thickness of background areas (~56 nm) slightly smaller than the particle diameter (~70 nm).
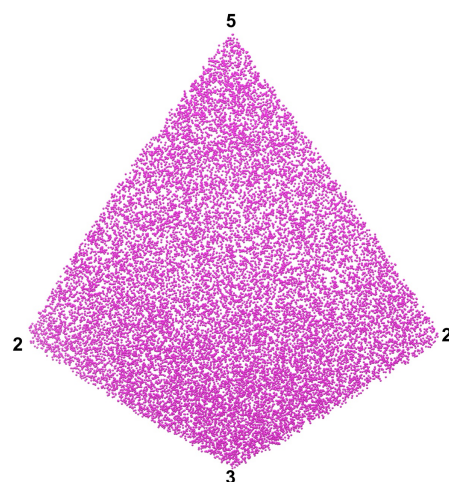

Figure s3. Euler angle distribution of TV particles captured by the antibody-based affinity cryo-EM grid. Figures "2", "3" and "5" represent the icosahedral two-, three- and five-fold axes, respectively.
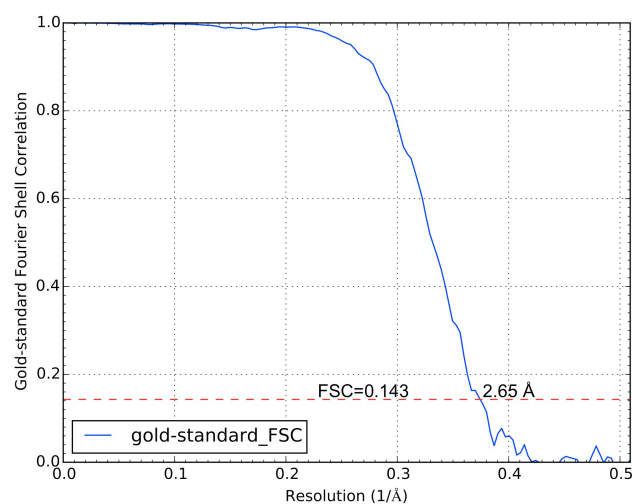
Figure s4. Gold-standard FSC curve of the 20S proteasome 3-D reconstruction with *jspr*.

The resolution was estimated at 2.7 Å using the 0.143 cutoff. The dataset was downloaded from

the public database EMPIAR (https://www.ebi.ac.uk/pdbe/emdb/empiar/entry/10025).